



Disinfection capability of Ag/g-C₃N₄ composite photocatalysts under UV and visible light illumination



Mario J. Muñoz-Batista*, Olga Fontelles-Carceller, Manuel Ferrer, Marcos Fernández-García, Anna Kubacka*

Instituto de Catálisis y Petroleoquímica, CSIC, C/Marie Curie 2, 28049 Madrid, Spain

ARTICLE INFO

Article history:

Received 29 July 2015

Received in revised form 6 October 2015

Accepted 12 October 2015

Available online 19 October 2015

Keywords:

Photo-catalysis

Carbon nitride

Silver

Sunlight

Biocide

Germicide

ABSTRACT

The biocidal capability of Ag/g-C₃N₄ composite photocatalysts against *Escherichia coli* was evaluated as a function of the Ag content of the material upon UV and visible light excitation. The Ag/g-C₃N₄ composite system shows significant biocidal activity, presenting a behavior with a strong dependence on the silver content as well as on the excitation wavelength. The physico-chemical characterization of the samples together with a Langmuir–Hinshelwood-type kinetic modelling of biocidal experiments and the (photoluminescence and electron paramagnetic resonance) analysis of charge handling properties of the solids were used to interpret the photocatalytic response of the composite materials. The overall analysis shows that the wavelength dependence observed for all Ag/g-C₃N₄ composite photocatalysts is strongly correlated with the semiconductor–metal heterojunction effect on charge separation, handling and recombination, indicating the key role of the cooperative action between the two components of the system. Such cooperative effect is studied along the sample series and discussed to be related to the efficient use of both hole and electron related species in the disinfection action.

© 2015 Elsevier B.V. All rights reserved.

1. Introduction

The biocidal action of semiconductors within the so-called advanced oxidation processes using light as the energy source of the process has been the subject of intensive research in the last decades. Light excitation of the semiconductor can generate energy-rich electron-hole pairs able to degrade chemicals and/or cell components of microorganisms, and rendering innocuous products, mainly water and carbon dioxide [1,2]. Anatase was the first semiconductor tested in the seminal works of Matsunga et al. [3,4], being subsequently the subject of a large number of studies summarized in recent reviews (see, for example, in [5–8]). A weak point of anatase is the need of UV light to generate charge pair carriers and thus its limited utility when visible light or, more importantly, sunlight are used in disinfection processes.

Among the possible alternatives which can profit from a wider (UV and visible) electromagnetic spectrum than anatase, the potential of carbon-based materials has been highlighted [2]. In particular, in very recent times the graphitic carbon nitride (g-C₃N₄) material has been analyzed in connection with biocidal

processes [9,10]. This polymeric semiconductor has a band gap energy of ca. 2.7 eV, making it as a viable photocatalyst for fruitful use of sunlight as a renewable energy source of biocidal processes. Such key property is combined with its low cost preparation as well as high thermal and chemical stability to render a very attractive functional material [11,12]. However, the biocidal action of g-C₃N₄ requires improvement mainly as a result of a relatively limited charge handling capability to generate chemistry at the surface [2,12,13]. This goal is commonly achieved through several methods including the doping of the semiconductor and/or the production of hetero-composite materials [2,9,13].

As the biocidal action of g-C₃N₄ has been suggested to be directly related to the nature and quantity of hole-related species located at the material [9,10], the use of electron withdrawing elements within a composite structure would strongly promote the effect of carbon nitride materials on microorganism viability. Among electron seeking components the use of metals and particularly silver have been pursued. Nanoparticulate silver by itself can have bactericidal activity, mostly based in a combination of the release of silver ions, the production of oxygen reactive species and, in specific cases, phagocytosis [14,15]. Moreover, the combination of silver with g-C₃N₄ provides an ideal situation with potential improvement of both components, as silver would be electron enriched while the semiconductor would be hole enriched, opening a way to enhancing simultaneously the biocidal capabilities of

* Corresponding authors. Fax.: +34 915854760.

E-mail addresses: mario.munoz@csic.es (M.J. Muñoz-Batista), ak@icp.csic.es (A. Kubacka).

both components. To the best of our knowledge, the silver-graphitic carbon nitride composite has been tested profusely for the photo-elimination of pollutants [16–25] but to date its biocidal potential has not been investigated and reported.

Here we will test the mentioned Ag/g-C₃N₄ composite system biocidal action upon both UV and visible light excitation in order to check the potential of the system in the most interesting UV and visible electromagnetic regions. To this end, we use the pathogenic *Escherichia coli* strain 1337-H as a target microorganism and consider the kinetic analysis of the photokilling tests as a suitable tool for interpreting the properties of the composite system in terms of the action of each component as well as of the system as a whole. The kinetic modelling of the results was carried out following (and modifying) the work of Marugan et al. [26,27]. Modeling of the inactivation profiles is grounded in a simplified (Langmuir–Hinshelwood-like multistep-type) reaction mechanism and considers that microorganism death occurs via a sequential attack of photo-radicals by which “undamaged” cells become “damaged” and eventually progress to an “inactivated” state. The utilization of an “adsorption Langmuir–Hinshelwood” type mechanism allows a reasonable and relatively flexible description of the inactivation. Moreover, the advantage of using this approach appears two-fold: first, (i) its usefulness in analyzing complete sets of inactivation profiles showing (or lacking) initial smooth/fast decays and final tailing section; and, more importantly, (ii) the model renders kinetic parameters allowing physical interpretation of the underlying process, in contraposition with many other simple kinetic laws used previously [26–29]. Such study is completed here with the characterization analysis of the fresh and used materials with the help of XRD, UV–vis and TEM, as well as with a photoluminescence/electron paramagnetic resonance study of the solids charge handling properties after excitation with all wavelengths used in the disinfection tests. With the help of this combined approach we can show that the behaviour of the system strongly depends on the excitation wavelength and pointed out the main physical causes to justify the biocidal properties of the materials.

2. Experimental

2.1. Catalysts preparation

The graphitic carbon nitride was obtained by calcination of melamine (Aldrich), in the semi-closed system (to prevent sublimation) at 580 °C with a heating ramp of 5 °C min⁻¹ for 4 h [30]. The composite materials were prepared using a single-pot microemulsion preparation method using *n*-heptane (Scharlau) as the organic medium, Triton X-100 (Aldrich) as a surfactant and hexanol (Aldrich) as a cosurfactant. The g-C₃N₄ was introduced into the organic phase of the microemulsion. After 30 min of stirring a certain quantity of AgNO₃ (0.5 M) aqueous solution was added into the organic phase. After 1 h, the adequate amount of a NaBH₄ aqueous solution (0.1 M) was quickly added into the solution under continuous vigorous stirring. Water/Ag and water/surfactant molar ratios were, respectively, 110 and 18 for all samples. The resulting mixture was stirred for 24 h and then centrifuged. The separated solid precursors were rinsed with ethanol, distilled water and acetone, and dried at 60 °C for 12 h. The sample names were xAg/g-C₃N₄ for the composite samples, where *x* is the wt.% (1, 2, 5 and, 10) of Ag with respect to g-C₃N₄.

2.2. Catalysts characterization

The BET surface areas and average pore sizes were measured by nitrogen physisorption (Micromeritics ASAP 2010). XRD profiles

were obtained with a Seifert D-500 diffractometer using Ni-filtered Cu K α radiation with a 0.02° step and fitted using the Von Dreele approach to the Le Bail method [31]; particle sizes were measured with XRD and evaluated using the Williamson–Hall formalism [32]. UV–vis diffuse reflectance spectroscopy experiments were performed with a Shimadzu UV2100 apparatus. Ag lixiviation at the liquid phase was measured in centrifuged, rinsed samples using Inductive Coupled Plasma-Mass Spectrometry (ICP-MS Nextion 300XX PerkinElmer).

The electron paramagnetic resonance (EPR) measurements were done with a Bruker ER200D spectrometer operating in the X-band and calibrated with a DPPH standard. For the 5,5-dimethyl-1-pyrroline *N*-oxide (DMPO) spin trapping EPR experiments, the samples were suspended in water or methanol (at a concentration of 0.6 g L⁻¹) and were sonicated for 4 min. A solution (0.01 M) of DMPO spin trap (supplied by Sigma) was prepared and kept on ice during the whole set of experiments. Bidistilled water (Elix-10) or methanol (Sigma) were employed for these preparations. 100 μ l of the solid suspension and 100 μ l of the DMPO solution were mixed into an EPR flat quartz cell under atmospheric air and irradiated at different times, through a spectroscopic Pyrex glass filter with a cut-off at ca. 220 nm, with light excitation source identical to that employed for the photokilling tests and allowing “monochromatic” radiation (± 20 nm half width), being then immediately transferred to the spectrometer cavity for EPR analysis. A small radical concentration decay (of ca. 5% on average) was observed in the dark during the course of spectrum recording. The latter were obtained at 298 K at ca. 9.75 GHz microwave frequency, 19.5 mW microwave power, 100 kHz modulation frequency, 1 G modulation amplitude and 2×10^5 spectrometer gain. No significant signal saturation was observed in those conditions. Blank experiments were also performed over mixtures of 100 μ l of the DMPO solution and 100 μ l of water or methanol to check the absence of radical formation in the absence of solid under the employed conditions.

2.3. Photocatalytic tests

The xAg/g-C₃N₄ samples together with blank tests (using either light without catalyst or the materials at dark conditions) were measured using the same bacterium inoculums (8.9 10^9 colony forming units (CFU) mL⁻¹) for all measurements reported. To prepare bacterial inoculum, cells of *E. coli* 1337-H were grown overnight at 37 °C with shaking at 200 rpm in 10 ml of Luria-Bertani broth (LB) overnight; then, 100 ml of LB medium were inoculated with 2 ml of the overnight culture, and the cells were grown for 4 h (at 37 °C) to 8.9 10^9 CFU mL⁻¹. As demonstrated by blank experiments, care was put of using a sub-lethal, maximum radiation energy fluence of ca. 1 kJ m⁻² throughout the study. Excitation of 1 ml inoculum was carried with a UV–vis spectrometer (Synergy HT Multi-Mode Reader–BioTek) equipped with filters to obtain “monochromatic” radiation (± 20 nm half width). After irradiation and for different time intervals, aliquots of 100 μ l were transferred to a 10 ml LB broth test tube. The order of cell dilution at this stage was 10⁻². Loss of viability after each exposure time was determined by the viable count procedure on LB agar plates after serial dilution (10⁻² to 10⁻⁵). All plates were incubated at 37 °C for 16 h after which they were scanned using a Bio-Rad Imaging System equipped with Analysis Software 4.6.5 (Bio-Rad) to enable enumeration of bacterial colonies among replicates. Detection limit of the automated method is below 10 colony units. Data reported in this contribution are typically the average of four to six different experiments. A minimum of four experimental runs was performed to determine antimicrobial activity.

2.4. Kinetic modelling

Modeling of the inactivation profiles was achieved, as mentioned, using an approach grounded in a simplified (Langmuir–Hinshelwood-like multistep-type) reaction mechanism based in three parameters; kinetic (k) and pseudo-adsorption (K) constants and an inhibition coefficient (n) [26]. The model considers that microorganism death occurs via a sequential attack of photo-radicals by which “undamaged” (denoted as u in subsequent equations) cells become “damaged” (denoted as d) and eventually progress to an “inactivated” state [5,26]. This leads to two differential equations as:

$$\frac{dN_u}{dt} = -k \frac{KN_u^n}{1 + KN_u^n + KN_d^n} \quad (1)$$

$$\frac{dN_d}{dt} = k \frac{KN_u^n - KN_d^n}{1 + KN_u^n + KN_d^n} \quad (2)$$

We modified this model by: (i) assuming a fast decay from “undamaged” to inactivated cells which would lead to a simplified mechanism with a single differential equation paralleling the one of a classical Langmuir–Hinshelwood mechanism:

$$\frac{dN_u}{dt} = -k \frac{KN_u^n}{1 + KN_u^n} \quad (3)$$

This simplification comes from the fact of the relative fast decay curves observed in our case due to the high activity of the systems as well as the experimental conditions ensuring that the whole water volume is exposed to light during the whole experiment [29].

Also, (ii) we modified the model to account the fact that pseudo-stationary tails are encountered at the end of the experiments. This can not be fully accounted by the above formulation(s) [26–29] which can handle tailing regions with slow variations but not pseudo-stationary conditions. The different tailing behaviour is related to the conditions (particularly the illumination of the whole volume and the consequent presence of significant amounts of cell debris) of the experiment rather than the catalyst performance [26–29]. In any case, pseudo-stationary conditions are typically observed in biocidal tests and previously treated using modified Chick–Watson, Hom or similar formulations [33]. However all these formulations lack interpretation in physical basis and here we show a satisfactory fitting of all experimental curves presented in this work can be achieved by assuming the presence of a fraction of bacteria inaccessible to the treatment (here called N_{in}). N_{in} is represented (in the most simple version as here tested) by a constant during the experiment in such a way that added to inactivated cells has to be equal to the initial, undamaged ones. The physical events taking place at the end of a biocidal test and their physico-chemical nature are discussed at length in following sections.

Numerical solution of the corresponding set of equations was achieved with a 5th order “adaptive size controlled” Runge–Kutta program, coupled to a Full Newton (non-linear fitting) algorithm in order to ensure the solution of the corresponding non-linear fitting problem [34]. Results reported here, e.g. in the specific reaction conditions used, concern the second model (single differential equation; Eq. (3)) as a better fit is obtained as judged by the coefficient of determination R^2 . Note nonetheless the trends among the catalysts series using both models were the same, indicating that interpretation of the results are independent of the model.

3. Results and discussion

A combination of results obtained with XRD and UV–vis tools was used to provide the main characterization data for the $xAg/g-C_3N_4$ samples. As shown by the X-ray diffractograms presented in Fig. 1, the $g-C_3N_4$ reference displays its characteristic pattern

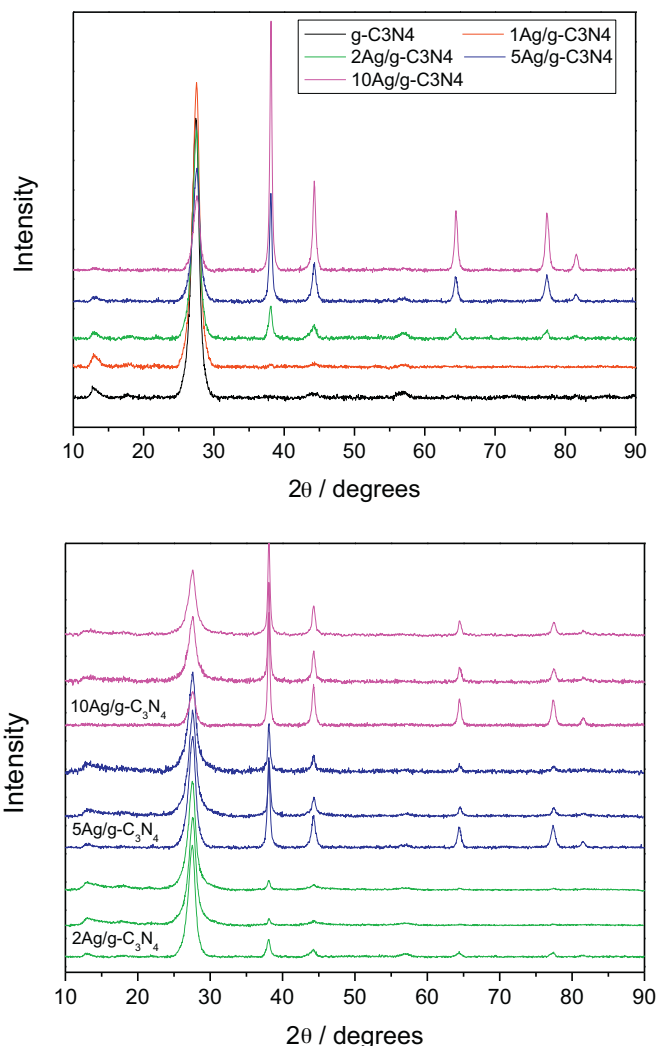


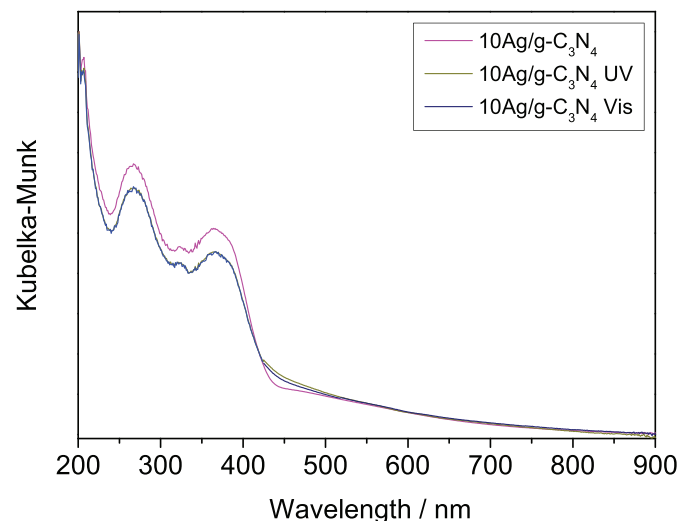
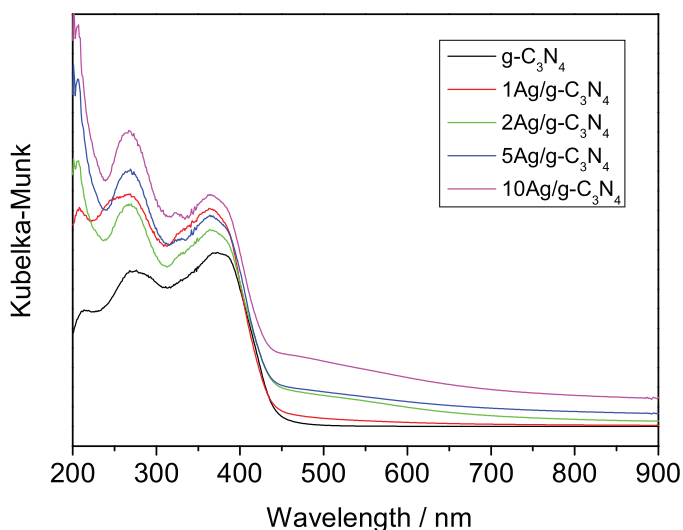
Fig. 1. XRD patterns of $xAg/g-C_3N_4$ samples and reference systems. Upper panel; fresh samples; Lower panel; comparison of fresh and used samples. For each sample patterns presented correspond to the fresh (lower), after UV use (middle) and after visible use (top) specimens.

dominated by the interlayer-stacking (002) reflection [35,36]. Additional, minor reflections are also observed among which the (100) interlayer reflection is the most intense. The $xAg/g-C_3N_4$ samples show patterns with a more or less constant contribution from the carbon nitride component but the characteristic Fm3m pattern (JCPDS card 04-0783; see Ref. [37]) of metallic silver was additionally detected in all cases. In fact, the silver contribution is barely observed for a 1 wt.% content but it is easily detected in the remaining samples. Table 1 summarizes the primary particle size of the silver component as well as the BET, pore size and volume though the $Ag-g-C_3N_4$ series. The silver particle size grows with the silver content of the composite from ca. 15 to 26 nm. At the same time, the silver–carbon nitride samples display, as expected, a nearly constant surface area ($13\text{--}17\text{ m}^2\text{ g}^{-1}$) and, in general, morphological properties. They are thus dominated by the main, graphitic carbon nitride component.

The optical properties of the composite samples were analyzed with the help of the UV–vis spectroscopy. The spectra, displayed in Fig. 2, are dominated by the $g-C_3N_4$ (the majority phase) light absorption capability in the UV and visible regions [35,36,38]. The presence of silver is nevertheless detected in the visible electromagnetic region, with the presence of a shoulder at the end of the sigmoidal decreasing shape at ca. 380–420 nm, the latter charac-

Table 1
Morphological properties for the xAg/g-C₃N₄ samples.^a

Sample	Ag fresh/used size (nm) ^b	Area BET (m ² /g)	Pore volume (cm ³ /g)	Pore size (nm)
g-C ₃ N ₄	–	13.7	0.087	27.0
1 Ag/g-C ₃ N ₄	15.1/15.4	12.4	0.085	35.9
2 Ag/g-C ₃ N ₄	15.7/16.3	15.3	0.091	25.8
5 Ag/g-C ₃ N ₄	21.8/22.9	18.7	0.111	25.0
10 Ag/g-C ₃ N ₄	25.9/27.8	17.1	0.098	23.7

^a Standard error: size 0.5 nm, BET 1.5 m g⁻¹; pore size 8%.^b Size of used samples correspond to UV aged specimens.**Fig. 2.** UV–vis spectra of xAg/g-C₃N₄ samples and reference systems. Upper panel, fresh samples; lower panel, 10 Ag/g-C₃N₄ sample before and after use under UV and visible light.

teristic of the carbon nitride band gap. A close look of the spectra indicates that the silver plasmon resonance is roughly peaking at the 510–530 nm region, in full agreement with previous reports for nanoparticulated silver [28,39,40]. In Table 2 we summarize the band gap of the Ag-g-C₃N₄ composite samples, presenting an average value of 2.80 eV, rather close to the pure carbon nitride reference, 2.71 eV. The value among xAg/g-C₃N₄ photocatalysts is essentially constant (within experimental error). Both facts indi-

Table 2
Carbon nitride band gap values for the xAg/g-C₃N₄ Samples.^a

Sample	Band gap (eV)		
	Fresh	After use 385 nm	After use 515 nm
g-C ₃ N ₄	2.71	2.70	2.71
1 Ag/g-C ₃ N ₄	2.81	2.72	2.73
2 Ag/g-C ₃ N ₄	2.75	2.72	2.73
5 Ag/g-C ₃ N ₄	2.81	2.82	2.82
10 Ag/g-C ₃ N ₄	2.85	2.87	2.86

^a Standard error: 0.05 eV.**Table 3**
Ag concentration at the liquid phase after biocidal tests.^a

Sample	Silver μg l ⁻¹	
	After use 385 nm	After use 515 nm
1 Ag/g-C ₃ N ₄	80.8	42.2
2 Ag/g-C ₃ N ₄	125.2	46.0
5 Ag/g-C ₃ N ₄	224.9	121.0
10 Ag/g-C ₃ N ₄	589.0	174.7

^a Standard error: 11%.

cate that silver has a limited influence in the optical properties of the major carbon-containing phase.

We completed the characterization of the xAg/g-C₃N₄ samples using transmission microscopy for selected samples. In Fig. 3 we present representative TEM images for the 10 Ag/g-C₃N₄ sample. Wide and detail views of the material are presented in the upper and middle row panels of the figure. The fine dispersion of the silver nanoparticles in the carbon nitride support appears evident. High magnification micrographs allow discerning crystallographic planes of the carbon nitride component but not of the Ag metallic particles (dark zones, chemical composition characterized by EDX) due to their instability under the electron beam. The analysis of the silver particle distribution is presented in Fig. 4. The plot shows a particle size distribution spreading from ca. 1 nm to more than 20 nm. The mean particle size of the fresh sample obtained after counting more than 200 particles is relatively small, 8.0 nm, but is qualitatively in agreement with the XRD-derived size as the corresponding volume–surface average mean size ($d_{4/3}$) is above 20 nm.

The multitechnique analysis allows thus to conclude that the composite samples display a reasonably dispersed silver component at the surface of the g-C₃N₄ phase. Silver nanoparticles grow moderately in size with the silver content while the morphology properties (BET and porosity) of samples are reasonably constant through the series. This comes out from the constancy of the major carbon nitride component which does not appear to be significantly modified by the presence of silver, as demonstrated by the XRD and UV–vis tools.

The activity of the xAg/g-C₃N₄ samples was tested in the elimination of *E. coli* under two representative excitation wavelengths; 385 nm for UV and 515 nm for visible. The first is a typical choice, allowing comparison with titania samples, while the second is fixed at the maximum intensity of the silver plasmon (measured with

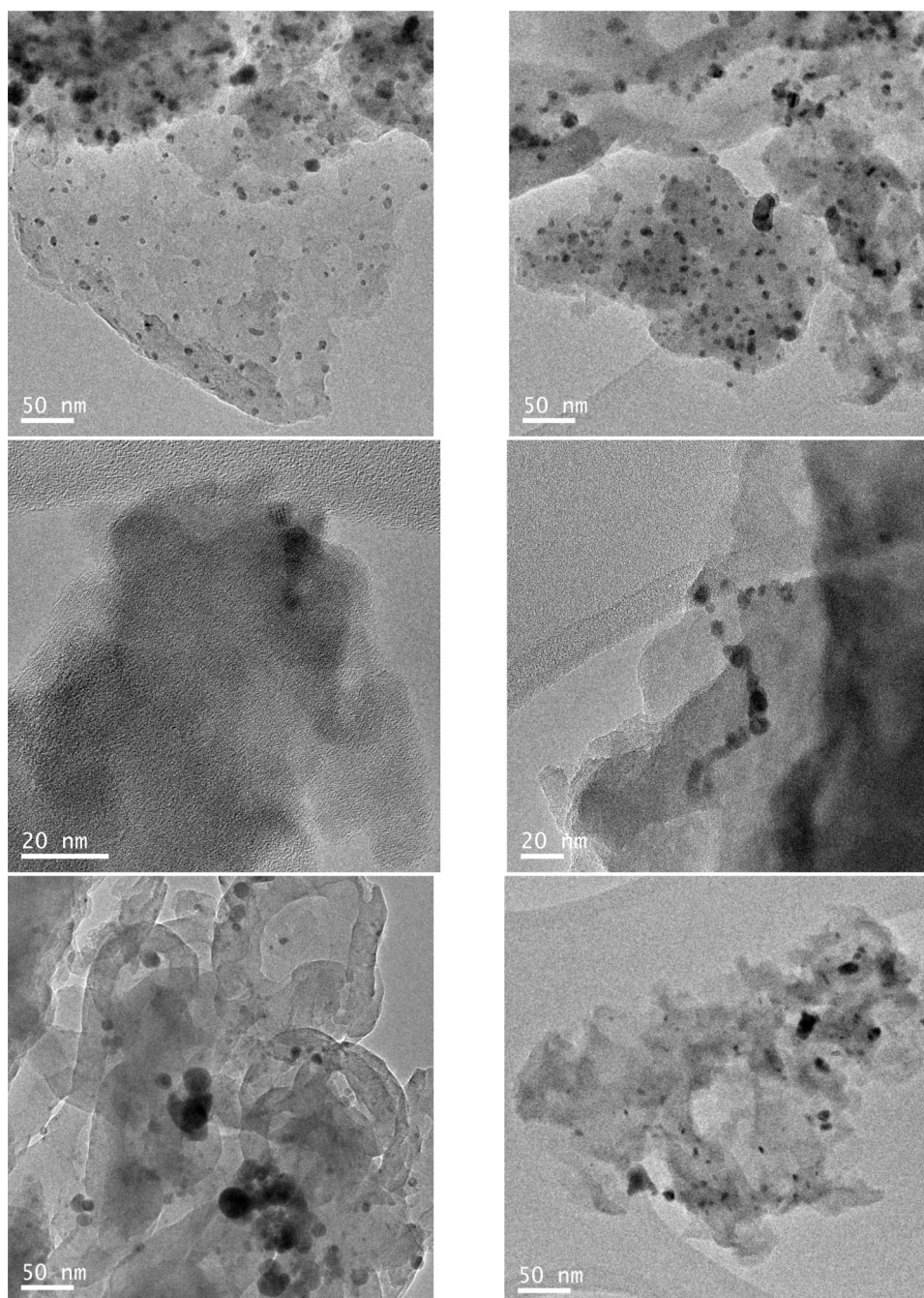


Fig. 3. Illustrative TEM images of the 10 Ag/g-C₃N₄ sample. Upper and middle row; fresh sample; Lower row; Sample after biocidal tests under 385 nm light excitation.

UV–vis spectroscopy, Fig. 2), allowing thus to calibrate the importance of this component in the overall disinfection properties of the system. Blank tests in absence of photocatalyst were also essayed, providing rather limited effects of the excitation light by itself. This is a direct consequence of the limited light intensity and fluence used in the experiments and has been previously discussed [41]. Dark experiments were performed with the sample having the highest silver loading to measure other than light-triggered biocidal effects. Again, a rather modest effect is observed in absence of light. The outcome of these tests is further discussed below.

The biocidal capability of the composite samples against *E. coli* is presented in Fig. 5 the higher activity presented by all samples under UV than visible light is evident (please, note the different ordinate scale in the two panels of Fig. 5). Upon UV excitation

the g-C₃N₄ reference shows significant activity and the addition of silver to the dominant carbon nitride component renders a complex behavior. For 1 and 2 silver wt.% samples the initial biocidal response is partially inhibited although by the middle of the experiment the response is higher than the reference. For larger loadings the microorganism viability decreases with respect to the reference results already from the beginning of the experiment. For the visible light experiments, the 1 and 2 silver wt.% samples do not differ significantly from the carbon nitride reference, being such differences clearly visible for higher loadings. Maximum activity is always detected for the 10 Ag/g-C₃N₄ sample, although the 5 Ag/g-C₃N₄ sample provides a rather close result.

To interpret the photokilling results Fig. 5 also presents results for the modeling work. As previously noted, the utilization of

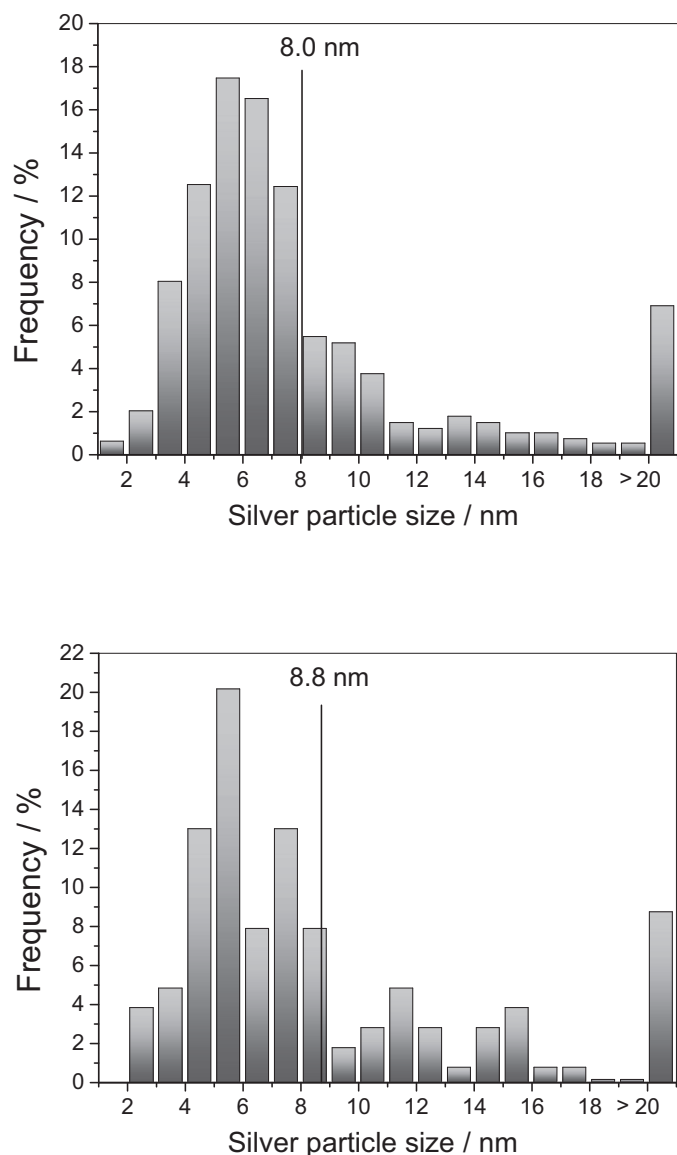


Fig. 4. Ag particle size distributions corresponding to the fresh (upper panel) and UV used (lower panel) 10 Ag/g-C₃N₄ sample. Note that particle sizes equal or above 20 nm are presented in a single bar.

an “adsorption Langmuir–Hinshelwood” type mechanism allows a reasonable and relatively flexible description of the inactivation profiles [26,28–30]. Note however that the complexity of the photo-activated disinfection process occurring once a microbe is in contact with a photogenerated radical means that we can talk of a “adsorption Langmuir–Hinshelwood” type mechanism where the complex set of elemental steps describing the process is crudely approximated. Still the model allows us to qualitatively differentiate between the relative importance of the adhesion and the radical attack processes. The presence of initial shoulders, inexistent under UV and only weakly detected under visible excitation, and/or tailing final regions are evident in a significant number of cases under study in Fig. 5. The fitting results also displayed in Fig. 5 render coefficient of determination (R^2) values above 0.997 and provide evidence of the goodness of the models which adequately describe the data in the whole time span of the experiment.

The output of the kinetic analysis of the biocidal tests is presented as full lines in Fig. 6. The initial step of the catalyst interaction with the microorganisms concerns the adsorption step [4–6,27,28,42,43]. We can see a more pronounced effect of the addi-

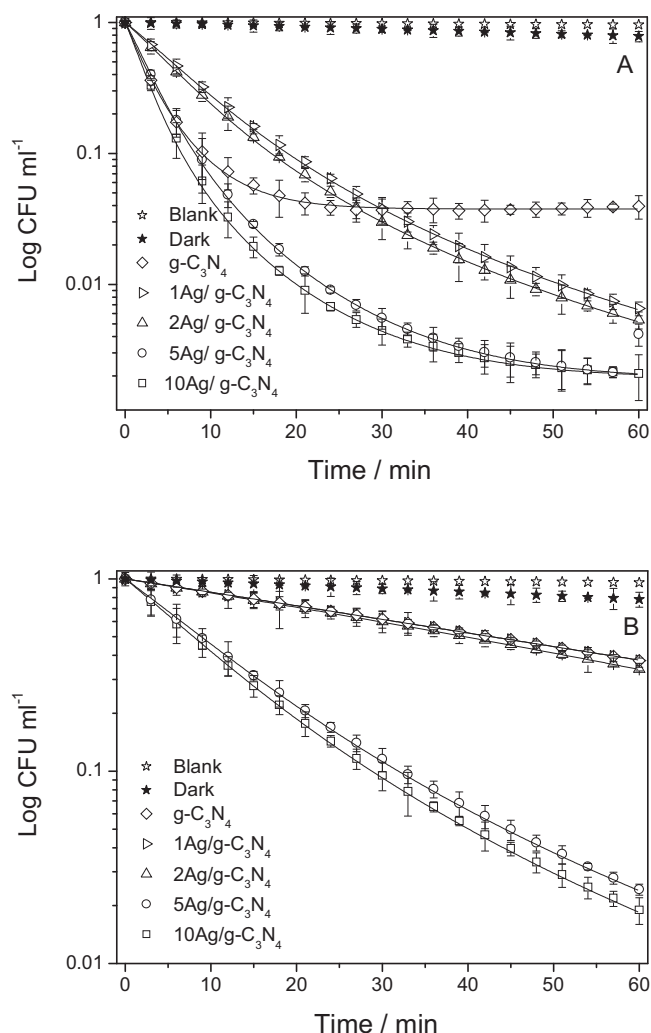


Fig. 5. Elimination profiles (scattered data) and kinetic modeling (dash line) for *E. coli* under 385 (UV; panel A) and 515 (visible; panel B) nm light excitation. The blank and dark tests reported in this figure were carried out, respectively, in absence of catalysts but in presence of light and in presence of the 10 Ag/g-C₃N₄ sample and absence of light.

tion of silver in the UV than in the visible light case but in all cases the values are higher than in the g-C₃N₄ reference. Contrarily to this result, the behavior of the kinetic constant is more complex. Under UV we can see a significant drop in magnitude in presence of 1 silver wt.% and a recovery for higher loadings. Such trend dominates and justify qualitatively the behavior observed in Fig. 5 for the Ag/g-C₃N₄ series. For visible light excitation the kinetic constant trend vs. silver content is similar to the one presenting the adsorption constant. The rationale behind the different behavior under UV and visible light excitation will be unveiled with the help of photoluminescence and electron paramagnetic resonance experiments.

Photoluminescence experiments are presented in Fig. 7 using the two wavelengths utilized as light sources in the biocidal experiments. Under a 385 nm light excitation, the g-C₃N₄ reference shows the broad, featureless peak at ca. 490 nm [11,12,36]. Silver presence decreases the photoluminescence intensity, providing evidence of a direct effect in charge recombination due to the well known ability of silver to actuate as an electron sink [1,2]. This will increase hole number and availability at the carbon nitride phase. The photoluminescence intensity decrease parallels the silver content. Under visible (515 nm) excitation we see decay curves with a potential,

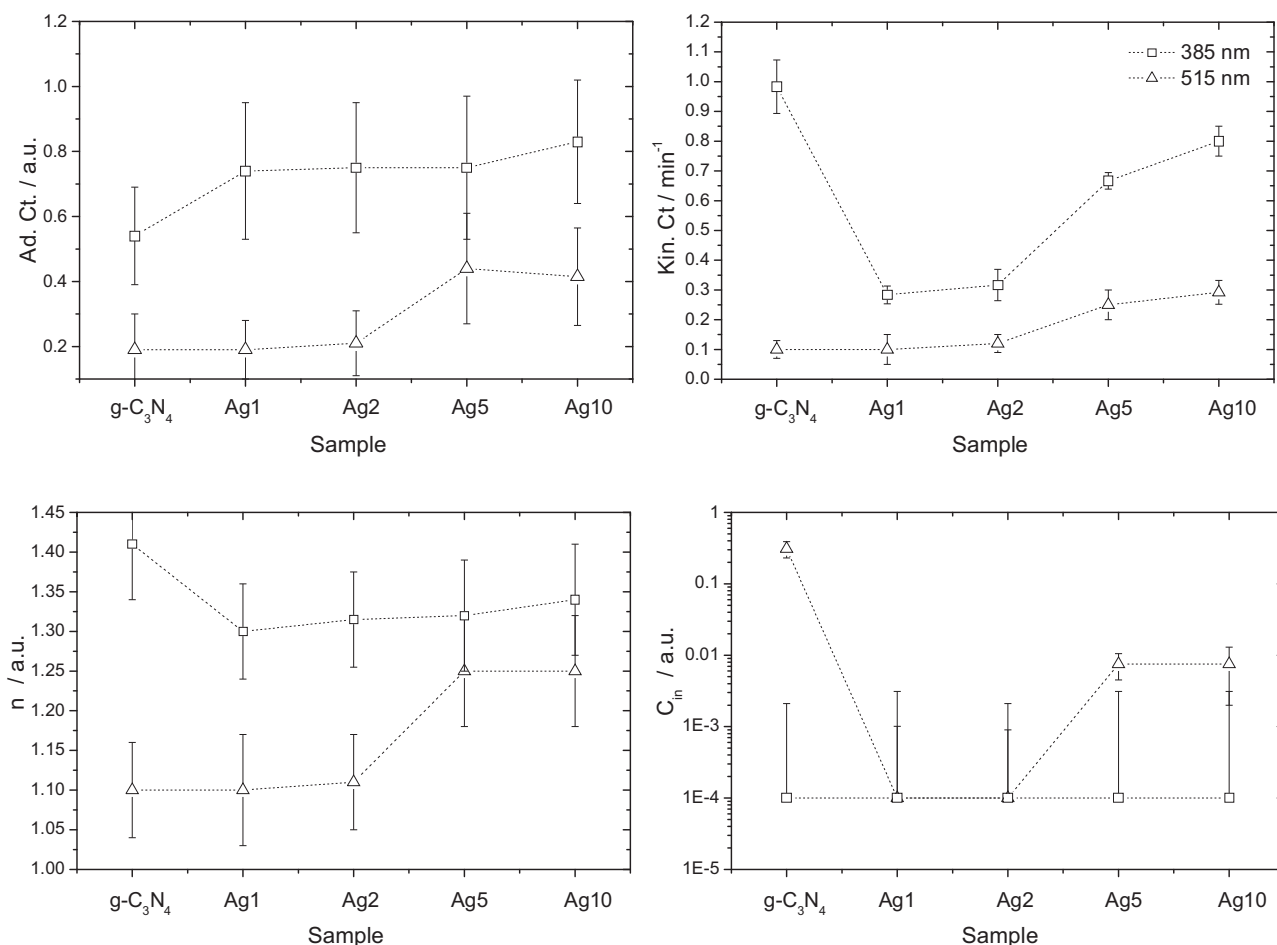


Fig. 6. Kinetic and adsorption constants, exponent coefficients, and fraction of inaccessible bacteria obtained from the kinetic analyses displayed in Fig. 5.

small peak at ca. 600 nm for the g-C₃N₄ reference. This would indicate the presence of localized gap states. Other peaks observed at higher wavelengths come from an incomplete elimination of the source features (due to their rather small intensity). This is demonstrated using silica or other large band gap “internal” samples (result not shown). Light absorption by silver would have mostly a non-radiative decay [2,39] and justify the essential absence of peaks in the lower panel of Fig. 7. In addition, the absence of noticeable photoluminescence intensity under visible excitation would indicate that electrons generated in silver do not interact strongly with the localized states of the carbon nitride component, although they are known to be flowed into the semiconductor conduction band [2]. Such process transfers electrons from the metal to the semiconductor under visible light excitation.

Using the combination of kinetic and photoluminescence we can discuss in a first approximation the biocidal action of the xAg/g-C₃N₄ samples. Although the photoluminescence indicate the higher availability of holes at the carbon nitride component in presence of silver, the kinetic analysis indicates a strong decay of the kinetic constant (Fig. 6). This may be at odds with the previously suggested critical effect of hole-related species in the biocidal capability of the g-C₃N₄ phase [9,10] and/or that a more complex mechanism with contribution of multiple radical species operate in the case of the composite system here analyzed. On the other hand, our results suggest a more decisive, positive influence of silver on adsorption capability of the samples. The adsorption constant depends on surface charge, hydrophobicity as well as the local effect generated by silver in neighboring surface adspecies [29,42,44,45]. The broad range of physical effects behind the adsorption constant makes its

analysis rather complex but in the Ag/g-C₃N₄ system, presence of silver is positive under UV excitation. For visible light excitation, the most critical effect is the net charge handling capability which, according to the UV-vis results (Fig. 2), is proportional to the silver content. The positive effect in both the kinetic and adsorption constants under visible excitation (Fig. 6) would indicate, in fact, that electrons would have a primary role in both physical events. This further suggests that both hole and electron charge carriers are involved in the biocidal action, likely within a complex mechanism to be elucidated with the help of in-situ techniques.

As a first step in such quest, here we use EPR. UV and visible irradiation of DMPO-containing sample water suspensions gives rise to two different signals. The most prominent is a signal with a 1:2:2:1 intensity pattern (panels A,C of Fig. 8). Its EPR parameters ($g = 2.0056$, $a_N = 14.9$ G, $a_H = 14.9$ G) are characteristic of DMPO-OH adducts generated by the reaction of the probe molecule and holes [28,40]. The accumulation of DMPO-OH radical adducts grows continuously in all cases but such radicals have a limited stability and a maximum concentration as a function of time is always detected. The latter is an effect of multiple additions, within consecutive reactions, of OH radicals to DMPO molecules to yield diamagnetic species [28,40,46–49]. The second signal has an odd number of peaks and is most likely indicative of an interaction of the unpaired electron with a hydrogen nucleus (panels A,C of Fig. 8). The DMPO-H adduct shows a 1:1:2:1:1:2:1:1 intensity pattern with EPR parameters as follows: $g = 2.0057$, $a_N = 16.6$ G, $a_H = 22.5$ G [50,51]. The experiments carried out using methanol as solvent (panels B,D of Fig. 8) show the formation of the DMPO-OOH adduct created by interaction of the probe molecule and the superoxide radical ($O_2^{\cdot-}$)

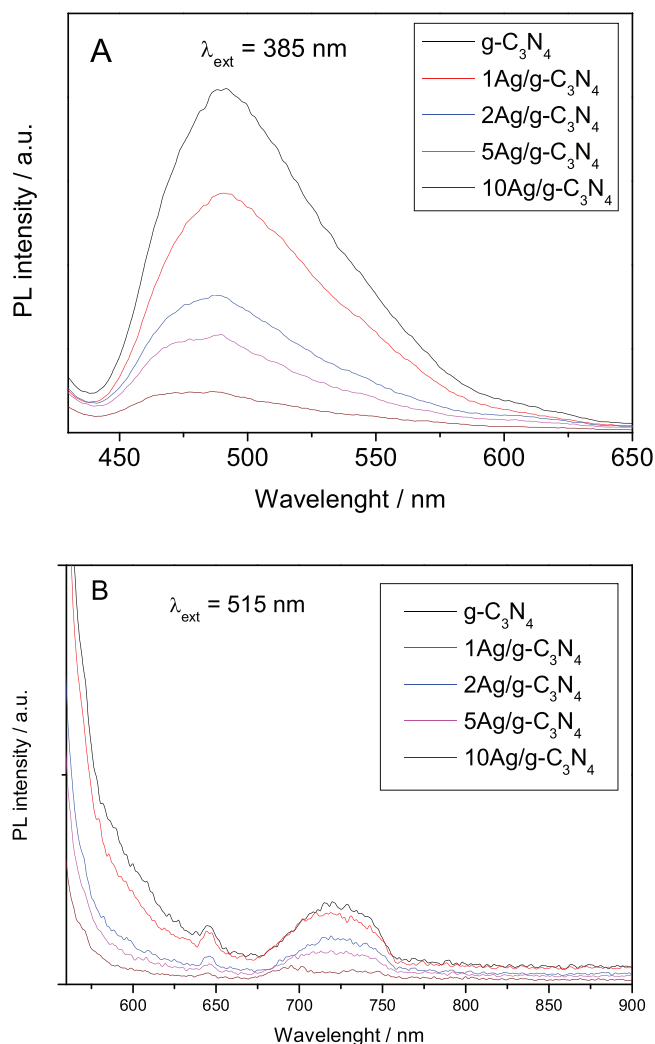


Fig. 7. Photoluminescence spectra of the $x\text{Ag/g-C}_3\text{N}_4$ samples. (A) $\lambda_{\text{ext}} = 385 \text{ nm}$, (B) $\lambda_{\text{ext}} = 515 \text{ nm}$.

Table 4

Values of initial rates of radical formation (r_{OH^\bullet} and r_{OOH^\bullet}) for the $10\text{Ag/g-C}_3\text{N}_4$ sample as measured with EPR.^a

	$\text{OH}^\bullet/385 \text{ nm}$	$\text{OH}^\bullet/515 \text{ nm}$	$\text{OOH}^\bullet/385 \text{ nm}$	$\text{OOH}^\bullet/515 \text{ nm}$
$r \left[\frac{\text{Number of spins}}{\text{min}} \right]$	2308	492	1948	177

^a Standard error: 20.5%.

and having EPR parameters such as $g = 2.0056$, $a_N = 13.1 \text{ G}$, $a_H = 12.1 \text{ G}$ [51,52]. The EPR experiments provide thus solid foundation for the hypothesis that the $\text{Ag/g-C}_3\text{N}_4$ samples are able to form both hole and electron related radical species under all (UV and visible) illumination conditions tested in this work.

As mentioned previously, due to the interaction of the spin probe with multiple radical species along the time, a safe comparison of results under the different illumination conditions should be thus carried out on the basis of the radical species initial formation rate. Fig. 9 provides the intensity evolution with time for the different EPR-active radical species and Table 4 reports the numerical values of the initial formation rates as measured by the corresponding slopes displayed as dashed lines in Fig. 9. This figure shows the different behavior of the different adduct species detected with EPR. While the DMPO-OH and DMPO-OOH adducts grow with time, indicative of their formation and evolution under illumination, the DMPO-H adduct is formed immediately after illu-

mination and essentially does not evolve. This fact indicates that the last adduct is not likely directly related to the photoactivity of the sample [28,40,46–52].

The rates of formation of radical species presented in Table 4 takes into account the weak signals (less than 2–4% of the signal obtained after 30 s under illumination) obtained at dark conditions, which were discounted from the values obtained under illumination. The rate values indicate the potential importance of both hole and electron related species under both UV and visible light illumination and thus provides the ground to our claim that both species would be of importance to interpret the photokilling activity of the samples. The comparison between the corresponding DMPO-OOH/DMPO-OH ratio gives a factor near 2.3 times superior under UV. This is further analyzed below.

The kinetic analysis is completed with the two parameters which concern the inactivation decay shown by the photocatalytic system at increasing reaction times. This would be related to “solid-poisoning” and/or “light shadowing” effects [5,26,29,33]. Solid-poisoning effects are accounted for the inhibition produced by the increasing concentration of cell debris and oxidation products appearing toward the end of the experiment and competing strongly for the radical species effectively eliminating microorganism and are quantified in our kinetic scheme by the inhibition coefficient (n) [5,26,29]. In Fig. 6 we plot evolution of the n coefficient. Higher values are observed under UV vs. visible excitation as a consequence of the larger activity in the former case. Changes among samples are of relatively moderate magnitude although the effect of silver is to decrease the inhibition effect under UV excitation but to increase under visible excitation. This may be due to the “reverse” electron flow direction observed under 385 vs. 515 nm light excitation. On the other hand, this inhibition effect is combined with the one mostly coming from a volume averaged shadowing effect roughly measured by the inaccessible fraction of microorganisms. The corresponding panel of Fig. 6 indicates that this effect is only operative under UV and for specific samples but its numerical value indicates a modest effect in the overall performance. In brief, deactivating effects are of moderate magnitude although the presence of silver has always a net positive effect under UV and a more complex behavior under visible excitation.

Fig. 6 and the above discussion would thus point out that the biocidal behavior vs. the silver content of the materials would be related to a complex trade-off that the generation and handling of both electron and hole charge carriers have in key physico-chemical events of the catalysts interaction with the microorganisms, including the adsorption, radical attack and, to a lesser extent, surface-poisoning effects. The final results is that a silver content of ca. 5 wt.% increases significantly the activity, with limited further increase in efficiency for higher loadings. The physico-chemical characterization indicates that the metal–support interface plays an important role in driving the disinfection capability of the $\text{Ag/g-C}_3\text{N}_4$ system. Under UV excitation, the electron and hole physical separation (at different solid phases) occurring after light excitation [8,9] is followed by the generation of a significant amount of the corresponding radical species of both charge carrier species at the surface of the material, according to the EPR experiments (Table 4). Under visible light, the electron flow from the metal to the semiconductor phase seems to be less effective in producing electron related radical species, likely by an effect of the trapping sites at the semiconductor, in comparison with hole-related species. The unravelling of the charge handling by the $\text{Ag/g-C}_3\text{N}_4$ requires however further study.

On the other hand, interesting to note is the evolution suffered by the samples during the biocidal tests. To examine the solid evolution we first used XRD and TEM to test the silver component stability. As shown in Figs. 1 and 4, silver maintains a dominant metallic state and displays a moderate growth of primary particle

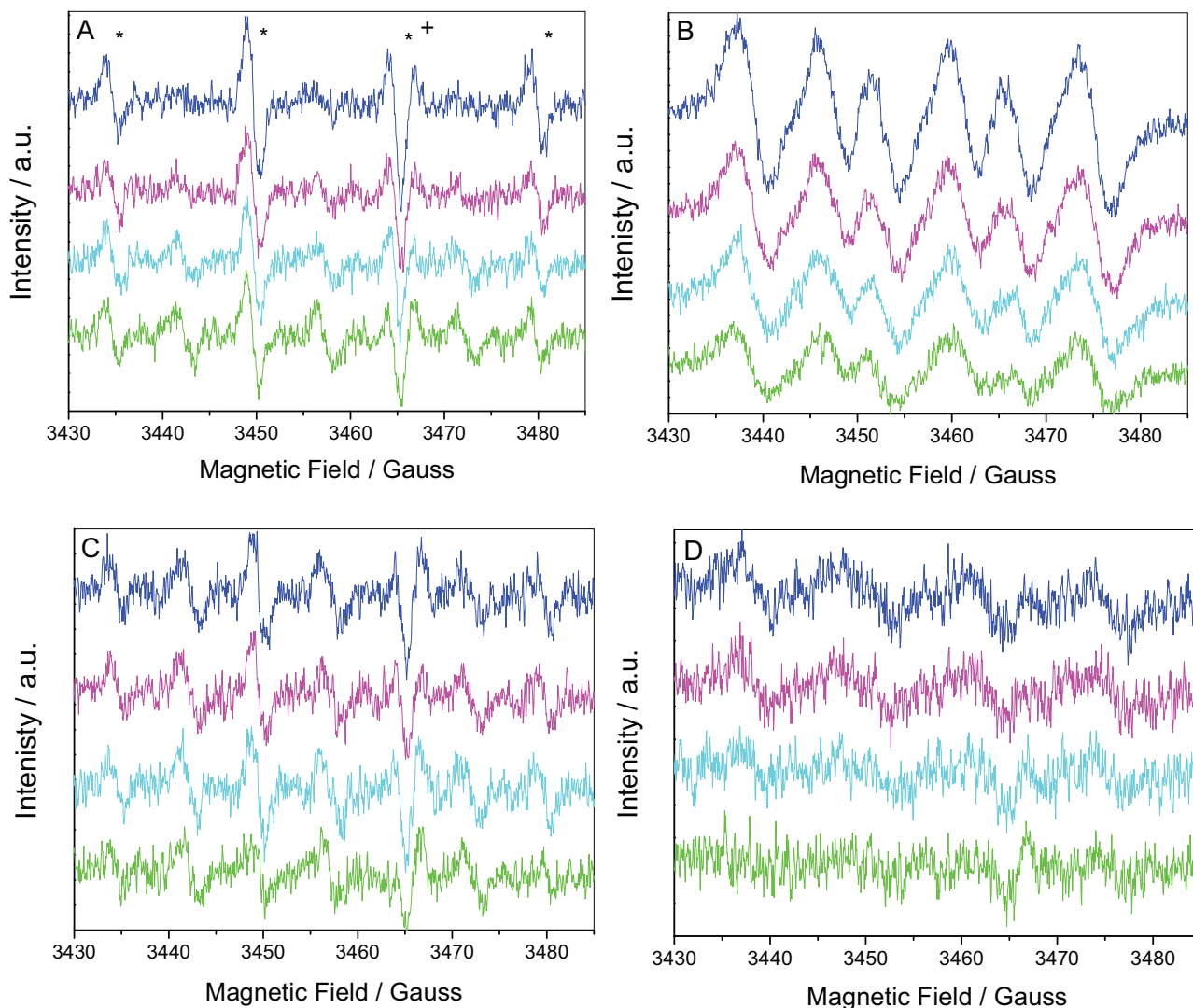


Fig. 8. (A,C) EPR spectra under UV (385 nm) and visible (515 nm) light irradiation, respectively, obtained after different time contact in presence of the 10 Ag/g- C_3N_4 material dispersed in water. The asterisk, sum mark the DMPO-OH signal and the cavity signal; (B,D) EPR spectra under UV (385 nm) and visible (515 nm) light irradiation, respectively, obtained after different time contact in presence of the 10 Ag/g- C_3N_4 material dispersed in methanol. From down to top: 1, 3, 5, and 10 min of time of contact.

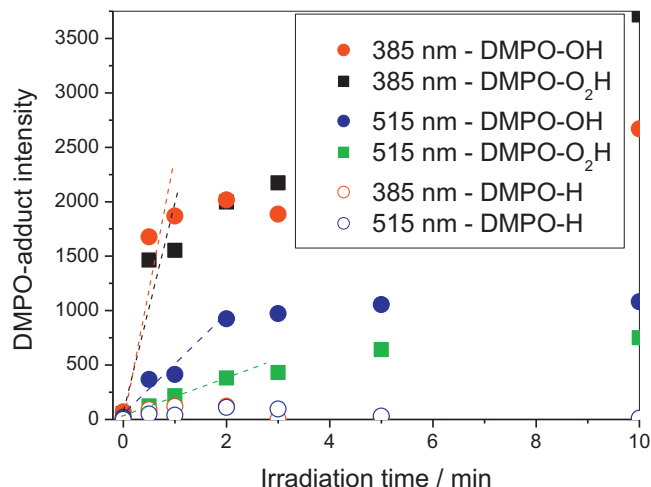


Fig. 9. Evolution of the radical species signal intensity for the experiments presented in Fig. 8 as a function of irradiation time using 385 and 515 nm excitation wavelengths. Lines correspond to the initial slope for radical formation.

size (Table 1) as a consequence of a variation in the primary particle size distribution which particularly depletes the presence of particles below 7 nm and increase the frequency of particles above 13 nm. Still the change in the noble metal average particle size is not very large, ca. of 1–2 nm (going from 0.5 for 1 Ag/g- C_3N_4 to ca. of 2 nm for 10 Ag/g- C_3N_4) in all samples. The silver particle size modification has also consequences in the UV-vis spectra; however as displayed in Fig. 2 they are of relatively minor significance in the noble metal plasmon resonance region, even for the largest silver loading here studied. In parallel, silver can evolve to the liquid phase by lixiviation. Table 3 shows that, in our experiments, silver is released in rather small quantities, below 0.1 % of the initial silver content for all samples. In addition, Table 3 points out that the liquid phase silver concentration reached by the end of the experiment is lower than the one required to render significant inactivation effects in *E. coli*. To be precise, absence of significant biocidal effects in the time span of our photokilling tests are typically observed for silver concentration at the liquid phase below 1–10 mg ml⁻¹ [53,54]. Moreover, as summarized in recent reviews, high biocidal activity for nanosilver materials is only achieved with a silver ion concentration at the liquid phase above ca. 500 $\mu\text{g l}^{-1}$ [55]. Only in the case of the 10 Ag/g- C_3N_4 sample under UV illu-

mination this limit is reached by the end of the experiment. The comparison of the photokilling activity of the $x\text{Ag/g-C}_3\text{N}_4$ ($x=5,10$) samples, having rather similar performance under all illumination conditions, would thus indicate the non-negligible but limited effect of silver lixiviation in the overall performance presented in Fig. 5. We can thus conclude that lixiviation is not having a significant influence in all conditions tested for the biocidal properties of the $x\text{Ag/g-C}_3\text{N}_4$ samples. Moreover, this discussion highlights the fact that the boosting of the silver capability in presence of the carbon nitride component comes out from the synergistic combination of the two solid components. The study of the system evolution at reaction conditions is completed with the analysis of the carbon nitride band gap value which is maintained constant for all samples within experimental error (Table 2). Overall, the characterization results indicate the reasonable stability of the $\text{Ag/g-C}_3\text{N}_4$ composite system and thus its adequacy for biocidal applications upon UV–vis electromagnetic excitation.

4. Conclusions

In this work we carried out an analysis of the biocidal capability of $\text{Ag-g-C}_3\text{N}_4$ samples as a function of the silver content and the excitation wavelength in the UV and visible light electromagnetic regions. To this end, we use a multitechnique approach combining XRD, UV–vis and TEM characterization techniques with a kinetic modelling of the biocidal results together with photoluminescence and EPR experiments.

Such analysis indicates that all samples evolve moderately under reaction conditions, mainly consisting in the aggregation of the silver component. Irrespective of the wavelength used to illuminate the samples, the composite system enhances the properties of both single components, providing a system with higher biocidal capability. Under UV the composite system is shown to handle charge carries more efficiently than the single components by effect of an efficient charge separation leaving hole-related radicals at the carbon nitride component and electrons at the noble metal one. This has a beneficial effect in the biocidal action. Under visible excitation, the silver plasmon resonance plays a role in the biocidal action. In both cases the synergistic interaction between the system components appears for loadings above 5 wt.% of silver and appears rooted in a complex combination of physico-chemical phenomena affecting adsorption, radical attack and, to a lesser extent, deactivation processes of the catalyst–microorganism interaction. Taking together the UV and visible photocatalytic results, they suggest that the biocidal action takes place through a complex mechanism with key involvement of both hole and electron related charge species. The feasibility of such hypothesis is supported by the EPR study of the radical species formed upon all illumination conditions tested in this work. Other potential contributions coming from lixiviation or silver alone (under dark conditions) effects are excluded to have a significant impact in the biocidal capability displayed by $x\text{Ag/g-C}_3\text{N}_4$ samples.

In summary, the study demonstrates that the $\text{Ag/g-C}_3\text{N}_4$ composite system displays a cooperative effect among components under illumination, providing a route (or routes) to improve the biocidal properties of carbon nitride and silver under light excitation. Such route(s) is (are) operative in the UV–vis (350–550 nm) electromagnetic region.

Acknowledgements

Financial support by Fundación General CSIC (“Programa Com-Futuro”) is acknowledged. M.J. Muñoz-Batista thanks “Ministerio de Economía y Competitividad” MINECO for support through the predoctoral FPI programme.

References

- [1] O. Carp, C.L. Huisan, A. Reller, *Prog. Solid State Chem.* 32 (2004) 33–104.
- [2] A. Kubacka, G. Colón, M. Fernández-García, *Chem. Rev.* 112 (2012) 1555–1604.
- [3] T. Matsunga, R. Tamada, H. Wake, *FEBS Microbiol. Lett.* 20 (1985) 211–224.
- [4] J.C. Ireland, P. Klostermann, E.W. Rice, R.M. Clark, *Appl. Environ. Microbiol.* 53 (1993) 1668–1679.
- [5] O.K. Dalrymple, E. Stefanakos, M.A. Trozt, D.Y. Goswamy, *Appl. Catal. B* 98 (2010) 27–76.
- [6] P.S.M. Dunlop, C.P.S. Sheeran, J.A. Bryne, M.A.S. McMahon, M.A. Boyle, K.G. McGuigan, *J. Photochem. Photobiol. A* 216 (2010) 303–312.
- [7] M.A. Mahmood, S. Baruah, A.K. Anal, J. Dutta, *Environ. Chem. Lett.* 10 (2012) 145–154.
- [8] W. Wang, G. Huang, J.C. Yu, P.K. Wong, *J. Environ. Sci.* 34 (2014) 232–247.
- [9] W.J. Wang, J.C. Yu, D.H. Xia, P.K. Wong, Y.C. Li, *Environ. Sci. Technol.* 47 (2013) 8724–8732.
- [10] J. Huang, W. Ho, X. Wang, *Chem. Commun.* 50 (2014) 4338–4342.
- [11] S. Cao, J. Low, J. Yu, M. Jaroniec, *Adv. Mater.* 27 (2015) 2150–2176.
- [12] Z. Zhao, Y.S. Liu, F. Dong, *Nanoscale* 7 (2015) 15–37.
- [13] Z.F. Jiang, D.L. Jiang, Z.X. Yan, K. Quian, J.M. Xie, *Appl. Catal. B* 170 (2015) 195–202.
- [14] S. Chermoussiva, M. Epplé, *Angew. Chem. Int. Ed.* 52 (2013) 1636–1653.
- [15] L. Rizzello, P.P. Pompa, *Chem. Soc. Rev.* 43 (2014) 1501–1518.
- [16] Y.L. Meng, J. Shen, D. Chen, G. Xin, *Rare Mater.* 30 (2011) 276–283.
- [17] L. Ge, C. Han, J. Lin, *Appl. Catal. A* 215 (2011) 409–415.
- [18] C. Cheng, Y. Fu, M. Hu, C.Y. Wang, G. Shan, L.Y. Zhu, *Appl. Catal. B* 142–143 (2013) 553–560.
- [19] Y.X. Yang, Y.N. Guo, F.Y. Liu, M.X. Huo, *Appl. Catal. B* 142–143 (2013) 828–837.
- [20] Y. Bu, Z. Chen, W. Li, *Appl. Catal. B* 144 (2014) 622–631.
- [21] X. Bai, R. Zhong, C. Li, D. Liu, Y. Liu, Y. Zhu, *Appl. Catal. B* 147 (2014) 82–91.
- [22] T. Zhou, Y. Xu, H. Wang, Z. Da, S. Huang, H. Ji, H. Li, *Ceram. Int.* 40 (2014) 9293–9301.
- [23] L. Ge, C. Han, J. Lin, *Appl. Catal. A* 409–410 (2015) 215–222.
- [24] X. Lu, J. Shen, J. Wang, Z. Cui, J. Xie, *RSC Adv.* 21 (2015) 15993–15999.
- [25] S.W. Hu, L.W. Wang, Y. Tian, X.L. Wei, J.W. Ding, J.X. Zhong, P.K. Chu, *Appl. Catal. B* 163 (2015) 611–622.
- [26] J. Marugán, R. van Grieken, C. Sordo, C. Cruz, *Appl. Catal. B* 82 (2008) 27.
- [27] J. Marugán, R. Van Grieken, C. Pablos, M.L. Satuf, A.E. Cassano, O.M. Alfano, *Appl. Catal. B* 102 (2011) 404–416.
- [28] A. Kubacka, M. Ferrer, M. Fernández-García, *Appl. Catal. B* 121–122 (2012) 230–238.
- [29] M.J. Muñoz-Batista, M. Ferrer, M. Fernández-García, A. Kubacka, *Appl. Catal. B* 154–155 (2014) 350–359.
- [30] M.J. Muñoz-Batista, M. Fernández-García, A. Kubacka, *Appl. Catal. B* 164 (2015) 261–270.
- [31] A. Le Bail, H. Duroy, J.L. Forquet, *Mater. Res. Bull.* 23 (1988) 447–456.
- [32] G.K. Williamson, W.H. Hall, *Acta Metall.* 1 (1953) 22–31.
- [33] M. Cho, H. Chung, J. Yoon, *Appl. Environ. Microbiol.* 69 (2003) 2284–2291.
- [34] J.E. Dennis, D.M. Gay, R.E. Welsh, (1981) *ACM Transactions on mathematical Software* 7 348 and 369.
- [35] S.C. Yan, Z.S. Li, Z.G. Zou, *Langmuir* 25 (2009) 10397–10403.
- [36] M.J. Muñoz-Batista, A. Kubacka, M. Fernández-García, *Catal. Sci. Technol.* 4 (2014) 2006–2015.
- [37] F. Witt, R.W. Vook, S. Luszcz, *Trans. Metall. Soc.* 242 (1968) 1111–1115.
- [38] M. Xiong, L. Chen, Q. Yuan, J. He, S.-L. Luo, C.T. Au, S.-F. Yin, *Dalton Trans.* 43 (2014) 8331–8337.
- [39] P.V. Kamat, *J. Phys. Chem. C* 111 (2007) 2834.
- [40] A. Kubacka, M.J. Muñoz-Batista, M. Ferrer, M. Fernández-García, *Appl. Catal. B* 140–141 (2013) 680–690.
- [41] A. Kubacka, C. Serrano, M. Ferrer, H. Lünsdorf, P. Bielecki, M.L. Cerrada, M. Fernández-García, M. Fernández-García, *Nano Lett.* 7 (2007) 2529.
- [42] J. Kiwi, V. Nadtochenko, *Langmuir* 21 (2005) 4631–4637.
- [43] B. Li, B.E. Logan, *Colloids Surf. B* 36 (2004) 81–92.
- [44] D. Gummy, C. Morris, P. Bowen, C. Pulgarin, S. Giraldo, R. Hazdun, J. Kiwi, *Appl. Catal. B* 63 (2006) 76–84.
- [45] N.J. Sucher, M.C. Carles, J. Nowotny, T. Bak, *Adv. Appl. Ceram.* 111 (2012) 16–45.
- [46] M.A. Grela, M.E.J. Coronel, A.J. Colussi, *J. Phys. Chem.* 100 (1996) 16940.
- [47] E.G. Janzen, N. Sankuraty, Y. Kotake, *J. Magn. Reson.* 111 (1996) 254.
- [48] M.D. Hernández-Alonso, A.B. Hungria, A. Martínez-Arias, M. Fernández-García, J.M. Coronado, J.C. Conesa, J. Soria, *Appl. Catal. B* 50 (2004) 167.
- [49] D. Dvoranova, V. Brezova, M. Mazur, M.A. Malati, *Appl. Catal. B* 37 (2002) 91.
- [50] C.F. Chignell, A.G. Motten, R.H. Sik, C.E. Parker, K. Reszka, *Photochem. Photobiol.* 59 (1994) 5–11.
- [51] Q. Chen, H. Shi, W. Shi, Y. Xu, D. Wu, *Catal. Sci. Technol.* 2 (2012) 1213–1220.
- [52] W. He, H. Jia, W.G. Wamer, Z. Zheng, P. Li, J.H. Callahan, J.-J. Jin, *J. Catal.* 320 (2014) 97–105.
- [53] A.K. Suresh, D.A. Pelletier, W. Wang, D.C. Joy, M.J. Doktycz, *Energy Sci. Technol.* 44 (2010) 5210–5215.
- [54] V. Del Lago, L.F. Oliveria, K.A. Gonzalves, J. Koberg, M. Cardoso, *J. Mater. Chem.* 21 (2011) 12267–12274.
- [55] M. López-Heras, I.G. Theodorou, B.F. Leo, M.P. Ryan, A.E. Proter, *Environ. Sci. Nano* 2 (2015) 312–326.